

Nematic and stripe orders within the charge density wave state of doped TiSe_2

Daniel Muñoz-Segovia,¹ Jörn W. F. Venderbos,^{2,3} Adolfo G. Grushin,⁴ and Fernando de Juan^{1,5}

¹Donostia International Physics Center, P. Manuel de Lardizabal 4, 20018 Donostia-San Sebastian, Spain

²Department of Physics, Drexel University, Philadelphia, PA 19104, USA

³Department of Materials Science and Engineering, Drexel University, Philadelphia, PA 19104, USA

⁴Institut Néel, CNRS and Université Grenoble Alpes, Grenoble, France

⁵IKERBASQUE, Basque Foundation for Science, Maria Diaz de Haro 3, 48013 Bilbao, Spain

(Dated: August 31, 2023)

In this work, we present a theory to reconcile conflicting experimental claims regarding the charge density wave (CDW) state in TiSe_2 , including whether there is a single or multiple CDW transitions and the occasional observation of rotation symmetry breaking. Using a $\mathbf{k} \cdot \mathbf{p}$ model coupled to the CDW order parameter, we show how commonplace conduction band doping x must cause a transition from the C_3 -symmetric $3Q$ state to a C_3 -breaking $1Q$ stripe state at a critical doping x_{1Q} . In addition, for sufficient ellipticity of the conduction bands, as displayed by the realistic band structure of TiSe_2 , a new nematic $3Q$ state also emerges in a region with $x < x_{1Q}$. We then show how both stripe and nematic states emerge from a minimal interacting tight-binding model, for both positive and negative initial gaps. Our theory clarifies a long-standing puzzle and its predictions can be verified with a variety of probes including transport, photoemission and tunneling.

Introduction.— The transition metal dichalcogenide TiSe_2 develops a commensurate $2 \times 2 \times 2$ charge density wave (CDW) transition below $T_c \sim 200\text{K}$ (shown in Fig. 1(a,b)), which has been under scrutiny for decades [1, 2]. Featuring nearly energetically aligned electron and hole pockets at the Brillouin Zone (BZ) L and Γ points (see Fig. 1(c,d)), TiSe_2 is naturally unstable to modulations with momentum $Q = \Gamma L_i$ which cause a repulsion of the electron and hole bands. These include both lattice modulations driven by electron-phonon coupling [3, 4] and charge modulations driven by excitonic correlations [5, 6], with both mechanisms likely contributing to the CDW [7–10]. While the microscopic interaction driving the CDW has been discussed at length, an even more pressing controversy regarding the symmetry of the CDW transition has received less attention and remains unresolved to date.

The CDW order parameter $\vec{\Delta}$, which has three components representing the three Q modulation vectors, was established by neutron diffraction [1] and X-ray [11] experiments to have L_1^- symmetry. These experiments further showed that $\vec{\Delta}$ condenses in a C_3 -symmetric $3Q$ configuration. This was later shown to be inconsistent with a Scanning Tunneling Microscopy (STM) experiment [12], where the CDW Bragg peaks at the three CDW wavevectors of the surface BZ \bar{M}_i displayed different intensities, thus breaking C_3 symmetry. Inspired by this, a chiral CDW breaking all mirrors, inversion and C_3 was proposed [13–16]. While further STM works [17, 18] provided support to this picture, others clearly displayed a C_3 -symmetric state [19]. X-ray and thermodynamic evidence for a second chiral transition were also reported [20], but the X-ray evidence was later contested [21, 22] and inversion symmetry breaking has never been established independently, as surface experiments [12, 17, 18] are insensitive to such symmetry.

The spontaneous breaking of threefold symmetry in the CDW Bragg peaks, once other artifacts such as tip anisotropy have been discarded [23], reflects a spontaneous electronic nematic order, as observed with STM for example in Kagome superconductors [24–26] or twisted heterostructures [27, 28].

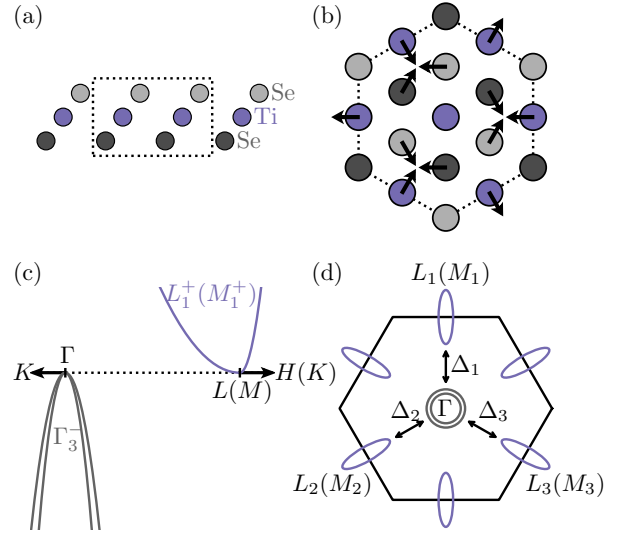


Figure 1. (a) Side view of the lattice structure of TiSe_2 . (b) Real space view of the charge density wave pattern. (c) Low energy band structure and symmetry labels for the bands for the bulk (notation in parenthesis for the monolayer). (d) Fermi surface sketch of the normal state in the semimetallic case. The order parameter $\vec{\Delta}$ coupling conduction and valence bands is also shown.

An inversion preserving nematic order is inconsistent with the chiral CDW proposal, and suggests an alternative explanation of the origin of C_3 symmetry breaking may exist. In this work, we offer a simple explanation that invokes only the standard L_1^- order parameter. We show that electron doping of the charge density wave state of TiSe_2 drives further electronic instabilities to C_3 -breaking states, first in the form nematic $2Q/3Q$ CDW states consistent with Refs. [12, 17, 18], and then as a $1Q$ stripe CDW at further doping. Actual samples of TiSe_2 are often doped to different degrees and only recently stoichiometric samples were achieved [29–31], which we believe explains the variability of symmetries observed. Our theory pertains

to the low-doping case only, $x < 0.06e/f.u.$, as higher levels of doping are known to first render the CDW incommensurate [32, 33] and then give rise to superconductivity [34, 35] as predicted theoretically [36–40].

Symmetry analysis and $\mathbf{k} \cdot \mathbf{p}$ model.— We begin by considering a continuum $\mathbf{k} \cdot \mathbf{p}$ model for the valence and conduction bands of TiSe₂, constrained by the symmetries of the high temperature phase (space group $P\bar{3}m1$, point group D_{3d}). The band structure near the Fermi level consists of three electron pockets at the L points with L_1^+ symmetry which derive from Ti d orbitals and two hole pockets of Γ_3^- symmetry located at Γ [41] which derive from Se p orbitals, as shown in Fig. 1(c,d). The presence of a small indirect gap ($E_g > 0$) or overlap ($E_g < 0$) is still debated [42–46], but our conclusions apply to both cases. The CDW order parameter has L_1^- symmetry and hybridizes the valence and conduction bands. In the case of monolayer TiSe₂, the electron pockets occur at the M points and have M_1^+ symmetry, resulting in an order parameter with M_1^- symmetry. Our proposed mechanism for rotation symmetry breaking applies to both monolayer and bulk samples with the corresponding replacement of the symmetry labels, so for simplicity we now focus on the monolayer.

The Hamiltonian H_{dd}^0 of the electron pockets, expressed in the basis $\{d_1, d_2, d_3\}$, where d_i represents the band at M_i , is:

$$H_{dd}^0(\mathbf{k}) = \text{diag}[\varepsilon_{d,1}(\mathbf{k}), \varepsilon_{d,2}(\mathbf{k}), \varepsilon_{d,3}(\mathbf{k})], \quad (1)$$

with $\varepsilon_{d,1}(\mathbf{k}) = a_d(k_x^2 + k_y^2) + b_d(k_x^2 - k_y^2)$, $\varepsilon_{d,2}(\mathbf{k}) = a_d(k_x^2 + k_y^2) + b_d[-\sqrt{3}k_x k_y - \frac{1}{2}(k_x^2 - k_y^2)]$, $\varepsilon_{d,3}(\mathbf{k}) = a_d(k_x^2 + k_y^2) + b_d[\sqrt{3}k_x k_y - \frac{1}{2}(k_x^2 - k_y^2)]$. The ellipticity of the electron pockets is parametrized by b_d , and the fact that the long axis is along ΓM requires $b_d > 0$. *Ab initio* calculations predict a large ellipticity value, $b_d/a_d \sim 0.87$ [37, 38, 47], which we take as the realistic value for the rest of this work. This value is also within the range of the experimentally reported conduction band masses (see Table III of the Supplemental Material (SM) [48]).

The hole bands at Γ are represented by the Hamiltonian H_{pp}^0 , which in the $\{p_x, p_y\}$ basis reads

$$H_{pp}^0(\mathbf{k}) = \begin{pmatrix} a_p k^2 + b_p(k_x^2 - k_y^2) & b_p 2k_x k_y \\ b_p 2k_x k_y & a_p k^2 - b_p(k_x^2 - k_y^2) \end{pmatrix}, \quad (2)$$

where b_p parametrizes the orbital texture of the hole bands. *Ab initio* calculations [41] show the top valence band has p_x character along the ΓM line (it is mirror M_x odd, becoming M_1^- at M), which sets $b_p < 0$. We take the value $b_p/a_p = 0.25$ from Refs. [37, 49].

Anticipating the CDW phase transition, we work in the folded BZ where the M point is folded to Γ . In the basis $\{d_1, d_2, d_3, p_x, p_y\}$, the bare $\mathbf{k} \cdot \mathbf{p}$ Hamiltonian is therefore

$$H^0(\mathbf{k}) = \begin{pmatrix} \frac{E_g}{2} + H_{dd}^0(\mathbf{k}) & 0 \\ 0 & -\frac{E_g}{2} + H_{pp}^0(\mathbf{k}) \end{pmatrix}, \quad (3)$$

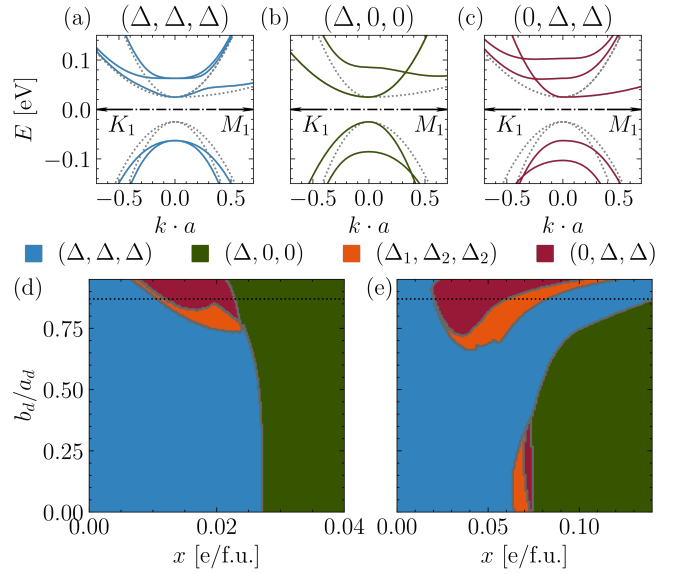


Figure 2. (a,b) Folded bands in the presence of the order parameter $\vec{\Delta}$ for directions (a) (Δ, Δ, Δ) , (b) $(\Delta, 0, 0)$, and (c) $(0, \Delta, \Delta)$. Grey dashed lines show the bands for $\vec{\Delta} = 0$. (d) Constant $|\vec{\Delta}|$ phase diagram for $E_g = +50$ meV and $|\vec{\Delta}| = 100$ meV as a function of electron doping x and ellipticity of the conduction bands b_d/a_d . The black dotted line indicates the realistic ellipticity $b_d/a_d = 0.87$. (e) The same as (d) but with $E_g = -100$ meV and on a larger x range.

where $\mathbf{k} = (k_x, k_y)$, and E_g is the gap, which is at most $|E_g| < 100$ meV. We do not consider spin-orbit coupling, because it does not significantly affect the CDW [50]. The bands of the model (3) are shown as grey dotted lines in Fig. 2(a,b).

Next, we consider the CDW order parameter with M_1^- symmetry, denoted $\vec{\Delta} = (\Delta_1, \Delta_2, \Delta_3)$, which couples the conduction and valence bands so that the total Hamiltonian becomes

$$H = \begin{pmatrix} \frac{E_g}{2} + H_{dd}^0(\mathbf{k}) & H_{dp}(\vec{\Delta}) \\ H_{dp}^\dagger(\vec{\Delta}) & -\frac{E_g}{2} + H_{pp}^0(\mathbf{k}) \end{pmatrix}. \quad (4)$$

This order parameter can be thought of as the M_1^- phonon displacement in normal coordinates, or as the excitonic order parameter of the same symmetry obtained from a mean-field decoupling. The lowest-order symmetry-allowed coupling is (see SM [48])

$$H_{dp}^\dagger(\vec{\Delta}) = \begin{pmatrix} \sqrt{\frac{2}{3}}\Delta_1 & -\frac{1}{\sqrt{6}}\Delta_2 & -\frac{1}{\sqrt{6}}\Delta_3 \\ 0 & \frac{1}{\sqrt{2}}\Delta_2 & -\frac{1}{\sqrt{2}}\Delta_3 \end{pmatrix}. \quad (5)$$

The C_3 -symmetric $3Q$ state [1] is represented by $\vec{\Delta} = \frac{|\vec{\Delta}|}{\sqrt{3}}(1, 1, 1)$. This order parameter causes a repulsion between the doublet of valence bands and a doublet of conduction bands (see Fig. 2(a)), leaving the band edge of the third conduction band unaffected by the CDW transition, as seen in ARPES [44, 46]. Figs. 2(b,c) show the bands for the $1Q$ $\vec{\Delta} = |\vec{\Delta}|(1, 0, 0)$ and $2Q$ $\vec{\Delta} = \frac{|\vec{\Delta}|}{\sqrt{2}}(0, 1, 1)$ states, respectively.

In the $1Q$ case, only one conduction band is repelled to high energies.

Energetics of the order parameter.— The CDW order parameter has three symmetry-related components, allowing for distinct ground states. Is the C_3 -symmetric $3Q$ state the ground state, and is it stable upon doping? These questions can be addressed within the continuum $\mathbf{k} \cdot \mathbf{p}$ model without knowledge of the precise nature or structure of the interaction that gives rise to $\vec{\Delta}$. Assuming an interaction that only depends on $|\vec{\Delta}|^2 = \Delta_1^2 + \Delta_2^2 + \Delta_3^2$, which holds when any local four-fermion interaction is decoupled only in the chosen channel, the direction of $\vec{\Delta}$ for fixed magnitude can be obtained at zero temperature by minimizing the energy of the occupied bands $E = \int d^2k / (2\pi)^2 \sum_n \varepsilon_n(\mathbf{k}) \theta(\mu - \varepsilon_n(\mathbf{k}))$ where $H\psi_n(\mathbf{k}) = \varepsilon_n(\mathbf{k})\psi_n(\mathbf{k})$. A phase diagram with approximate phase boundaries (compared to a self-consistent calculation of $\vec{\Delta}$) can thus be obtained to explain the origin of the different phases.

In Fig. 2(d) we show such a phase diagram for fixed $|\vec{\Delta}|$ and $E_g > 0$, as a function of doping x and conduction band ellipticity b_d/a_d . We vary a_d to keep the bare density of states (DOS) $\rho = 1/(4\pi\sqrt{a_d^2 - b_d^2})$ constant, to emphasize the role of ellipticity. Three main phases are observed. The C_3 -symmetric $3Q$ state is the ground state at stoichiometry for any b_d , as expected. For moderate values of $b_d/a_d < 0.7$, there is a sharp $3Q$ to $1Q$ transition at a critical doping x_{1Q} . In addition, at higher values of b_d/a_d , a nematic $3Q$ phase emerges where $|\vec{\Delta}| = (\Delta_1, \Delta_2, \Delta_2)$, with $|\Delta_1| \neq |\Delta_2|$. Further increasing b_d/a_d , Δ_1 vanishes and the nematic phase becomes $2Q$ with $|\vec{\Delta}| = (0, \Delta, \Delta)$. This $2Q$ state is distinguished from the nematic $3Q$ because it preserves an extra inversion symmetry in the center of the Ti-Ti bond [48].

The emergence of the $3Q$ to $1Q$ transition can be understood most clearly in the isotropic case $b_p = b_d = 0$, for which the energies of the two phases can be computed and integrated analytically (see SM [48]). This yields a critical doping which takes the simple form $n_{1Q} = \frac{|\vec{\Delta}|}{\pi} \sqrt{\frac{\log 2}{3a_d(a_d - a_p)}}$ in the $E_g = 0$ limit. To see that a transition from the $3Q$ to the $1Q$ state should occur at some critical doping, consider the effect of adding carriers on the energies of these states. In the $1Q$ state two bands are populated as carriers are added, whereas in the $3Q$ state only one band is populated by additional carriers, as can be seen in Fig. 2(a,b). This implies a higher chemical potential for the $3Q$ state and an energy which increases faster relative to the $1Q$ state, eventually making the latter lower in energy. This mechanism is still at work at finite b_d , as we observe numerically.

To understand the origin of the $3Q/2Q$ nematic phase, Fig. 3(a) shows a close up of the dispersion of the lowest conduction band ε_{c1} along ΓM as a function of b_d for fixed a_d and $\vec{\Delta} = \frac{|\vec{\Delta}|}{\sqrt{3}}(1, 1, 1)$. Fig. 3(b) shows the corresponding DOS. Increasing the ellipticity first produces a kink in the dispersion (a relative minimum of $d\varepsilon_{c1}/dk_y$), which eventually gives rise to a van Hove singularity (vHs) with diverging DOS. When the filling is close to that of the six symmetry

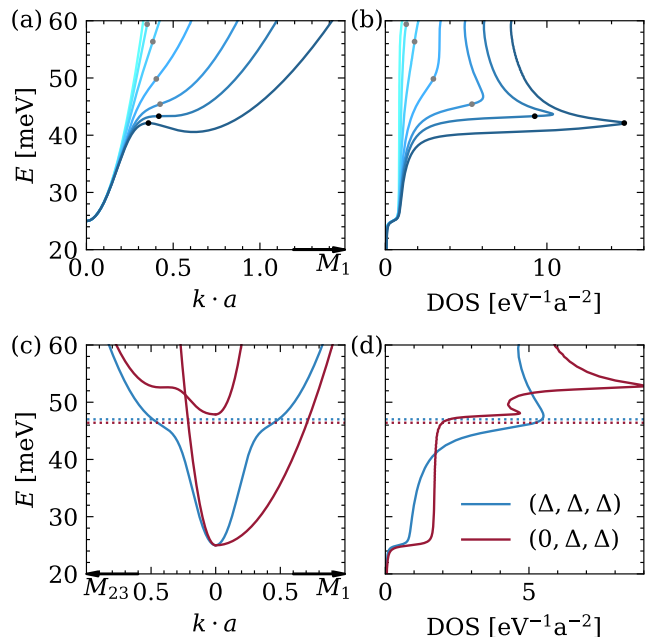


Figure 3. (a) Lowest conduction band along the ΓM direction and corresponding DOS in the C_3 -symmetric $3Q$ phase with $E_g = +50$ meV and $|\vec{\Delta}| = 100$ meV for constant a_d and ellipticities $b_d/a_d = 0, 0.39, 0.60, 0.78, 0.88, 0.92, 0.95$. A kink in the band is signaled by gray dots, and a van Hove singularity by black dots. (b) Corresponding DOS for each band in (a). (c) Conduction bands along the ΓM_1 and ΓM_2 directions (ΓM_3 is equivalent to ΓM_2) in the C_3 -symmetric $3Q$ (blue) and nematic $2Q$ (red) phases with $E_g = +50$ meV, $|\vec{\Delta}| = 100$ meV and $b_d/a_d = 0.87$. Horizontal dotted lines indicate the chemical potentials for $x = 0.0182$, where the C_3 -symmetric $3Q$ phase is unstable towards the $2Q$ state. (d) Corresponding DOS for each band in (c). The three equivalent vHs singularities of the lowest conduction band in the symmetric $3Q$ state disappear in the $2Q$ state, which has higher DOS at lower energy and therefore lower total energy.

equivalent vHs points, breaking the C_3 symmetry can lower the energy by splitting these saddle points in energy, a known mechanism for nematicity in the doped honeycomb lattice [51] and in Kagome superconductors [52]. Indeed, such splitting is observed in Fig. 3(c,d) in the nematic state, explaining its origin. In Fig. 2(d), this $3Q/2Q$ nematic phase develops even at values of b_d where the vHs singularity is not fully developed and there is only a finite but sizable DOS peak. Eventually, for higher doping, the $1Q$ stripe phase always develops.

Fig. 2(e) shows the phase diagram for $E_g = -100$ meV, with the following differences with respect to $E_g > 0$. First, there is an intermediate nematic $3Q/2Q$ state also at small ellipticity, which occurs at fillings where the second conduction band, of approximate mexican hat shape for $\vec{\Delta} = \frac{|\vec{\Delta}|}{\sqrt{3}}(1, 1, 1)$, begins to be populated. Since the DOS is also large there, a similar mechanism as the one for large ellipticity drives the transition to the nematic $3Q/2Q$ phase. Furthermore, at high ellipticity, including $b_d/a_d \sim 0.87$, a reentrant C_3 -symmetric $3Q$ phase appears between the nematic $3Q$ state and the $1Q$

stripe phase. In this region, the doping is well above the vHs, so that no nematic instability occurs, but the $1Q$ state energy is still higher. This reentrant phase shows that the mechanisms for the $1Q$ and $2Q/3Q$ nematic states are generically different.

Minimal lattice model with interactions.— The continuum $\mathbf{k} \cdot \mathbf{p}$ model provides a compelling basic understanding of the CDW phase diagram as a function of doping, purely based on energetic considerations. To obtain a more refined understanding based on a model which includes microscopic interactions, we now consider a tight-binding lattice model and study its ground state phase diagram within Hartree-Fock theory. We construct a minimal tight-binding model which accurately captures the band dispersion and eigenstate symmetry near the Fermi level and reproduces the low-energy $\mathbf{k} \cdot \mathbf{p}$ model when expanded near Γ and M . As such, the tight-binding model can be viewed as a lattice regularization of the $\mathbf{k} \cdot \mathbf{p}$ model. Furthermore, the tight-binding model breaks the artificial independent conservation of the charge of the conduction and valence bands present in the $\mathbf{k} \cdot \mathbf{p}$ model.

Our minimal lattice model is a three-orbital model, with d_{z^2}, p_x, p_y orbitals sitting at the same 2D triangular lattice sites. The d_{z^2} orbital transforms as A_{1g} and constitutes the conduction band, whereas the p_x, p_y orbitals transform as E_u and form the valence bands. We include hoppings up to third nearest neighbours for d_{z^2} , nearest neighbour σ and π hopping for p_x, p_y , and an interorbital hopping t_{dp} :

$$H_0 = \sum_i \left(\varepsilon_d d_i^\dagger d_i + \varepsilon_p \mathbf{p}_i^\dagger \cdot \mathbf{p}_i \right) + \sum_{n=1}^3 \sum_{\langle ij \rangle_n} t_{dd}^{(n)} d_i^\dagger d_j - \sum_{\langle ij \rangle_1} \left[(t_{pp\sigma} + t_{pp\pi}) (\mathbf{p}_i^\dagger \cdot \hat{\mathbf{r}}_{ij}) (\hat{\mathbf{r}}_{ij} \cdot \mathbf{p}_j) - t_{pp\pi} \mathbf{p}_i^\dagger \cdot \mathbf{p}_j \right] - \sum_{\langle ij \rangle_1} i t_{dp} \left(d_i^\dagger \hat{\mathbf{r}}_{ij} \cdot \mathbf{p}_j - h.c. \right). \quad (6)$$

Here $\langle ij \rangle_n$ are the n^{th} nearest neighbours, $\mathbf{p}_i = (p_{xi}, p_{yi})$, and $\hat{\mathbf{r}}_{ij} = (\mathbf{r}_j - \mathbf{r}_i) / |\mathbf{r}_j - \mathbf{r}_i|$ is the unit vector from site i to site j . As described in the SM [48], the hopping parameters are fit to reproduce the gap and masses of the bands near the Fermi level (see the inset of Fig. 4 for the bands for $E_g = 0$).

The CDW order in this model is represented by the local p - d hybridization, encoded in the fermion bilinear $\langle d_j^\dagger p_{\alpha j} \rangle$, with $j = 1, \dots, 4$ running over the sites of the 2×2 supercell, which transforms under symmetry as $\Gamma_3^- \oplus M_1^- \oplus M_2^-$. We now complete the model with the most local interaction that is attractive only for the M_1^- channel, which is

$$H_{\text{int}} = V_{dp} \sum_{\langle ij \rangle_1} \left(d_i^\dagger \mathbf{p}_i \right)^\dagger \cdot (1 - 2\hat{\mathbf{r}}_{ij} \otimes \hat{\mathbf{r}}_{ij}) \cdot \left(d_j^\dagger \mathbf{p}_j \right), \quad (7)$$

with $V_{dp} > 0$. The time-reversal even M_1^- component of $-2V_{dp} \langle d_j^\dagger p_{\alpha j} \rangle$ defines the order parameter and is given explicitly by

$$\Delta_a = -V_{dp} \sum_j e^{i\mathbf{M}_a \cdot \mathbf{r}_j} \text{Re} \langle d_j^\dagger \mathbf{p}_j \rangle \times \frac{\mathbf{M}_a}{|\mathbf{M}_a|}, \quad (8)$$

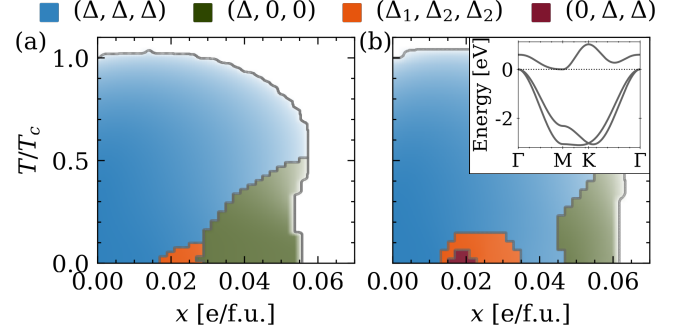


Figure 4. Temperature-doping phase diagrams for positive and negative gaps: (a) $E_g = +25\text{meV}$, $V_{dp} = 845\text{meV}$; (b) $E_g = -35\text{meV}$, $V_{dp} = 716.5\text{meV}$. The intensity of the color of each phase is proportional to $|\bar{\Delta}|$. Critical temperatures at charge neutrality are (a) $T_c = 459\text{K}$ and (b) $T_c = 239\text{K}$. The inset shows the band structure of the tight-binding model in the unfolded unit cell for $E_g = 0$.

where $a = 1, 2, 3$ and $\mathbf{v} \times \mathbf{w} = v_x w_y - v_y w_x$. The mean field decoupling of Eq. (7) indeed shows that it is only attractive in this channel, and that $\bar{\Delta}$ couples to electrons and holes as in Eq. (4) at low energies as desired (see SM [48]). Our interacting TB Hamiltonian therefore serves as a minimal model to analyze the energetics of the M_1^- CDW order.

We perform self-consistent mean-field calculations of the Hamiltonian $H_0 + H_{\text{int}}$ decoupled in the $\langle d_j^\dagger p_{\alpha j} \rangle$ channels for different values of the initial gap. We choose V_{dp} such that the critical doping for the disappearance of the commensurate CDW is $\sim 6\%$, as determined experimentally [32, 35, 46, 53].

Figs. 4(a,b) display the resulting phase T - x diagrams for gaps $E_g = +25\text{meV}, -35\text{meV}$. States (Δ, Δ, Δ) , $(\Delta_1, \Delta_2, \Delta_2)$, and $(\Delta, 0, 0)$ appear for both gaps, while a $2Q$ $(0, \Delta, \Delta)$ phase develops only in the negative gap case. At zero temperature, the C_3 -symmetric $3Q$ phase (Δ, Δ, Δ) appears at low doping, while the $1Q$ -stripe order only develops at high doping, with the nematic $3Q/2Q$ phase developing in between, in agreement with Fig. 2(d,e). When the gap is negative, the reentrant C_3 -symmetric $3Q$ phase is also observed between the nematic $3Q$ and the $1Q$ phases. Starting from high temperature, the first transition is always to the C_3 -symmetric $3Q$ phase. At high doping, the $1Q$ phase develops at a lower but comparable temperature. On the other hand, the nematic $3Q/2Q$ phase only appears at low temperature ($T_{\text{nematic}} \sim 0.2 T_{\text{CDW}}$), which is expected for a secondary instability of the $3Q$ CDW state.

Bulk TiSe₂.—Our calculations assume a monolayer for simplicity, but we expect the existence of doping-induced transitions to carry over to the bulk limit, because TiSe₂ is a quasi 2D van der Waals material with weak band dispersion in the k_z direction. In the bulk, the order parameter has L_1^- symmetry, which preserves the inversion center between layers. Because of this, none of the bulk versions of our proposed states is chiral, differentiating them from previous proposals [13–16] to explain the C_3 -breaking states [12, 17, 18]. We caution

however that since STM is a surface probe and doping need not be homogeneous, the bulk and surface CDW states need not be the same. We also note that short-range domains of a $1Q$ stripe CDW [54] in a $3Q$ background have also been observed. Modeling phase coexistence in such inhomogeneous states is beyond the scope of this work but our predicted $1Q$ stripe phase at high doping is a good starting point.

Bulk samples cooled in the presence of circularly polarized light display a longitudinal circular photogalvanic effect which is consistent with C_3 symmetry [55, 56]. This light-induced chiral state is therefore different from our proposal, and is likely induced by the condensation of phonons with M_1^- symmetry [57] (which is not the leading bulk instability) aided by the presence of circular light. By including the coupling to circularly polarized light, our theory could be generalized to address this case, but we emphasize that this light-induced chiral state is unrelated to the one observed in STM. It is also worth noting that the mixing of M_1^- and L_1^- phonons has been predicted to stabilize C_3 -breaking structures as well [58].

Discussion.— Our prediction of a robust, doping induced C_3 -breaking phase in TiSe_2 , motivated by different STM experiments, can solve the long-standing puzzle of the symmetry of the CDW. Our theory can be further confirmed with several other probes. The existence of a nematic transition can be quantified by elastoresistance measurements which directly measure the nematic susceptibility. An early experiment [59] indeed detected a sharp change in elastoresistance below 200 K. C_3 -breaking can also be detected in low frequency Raman as observed in 2H-TaSe_2 [60]. ARPES experiments may also detect different intensity for the three conduction band pockets in the C_3 breaking states. Another unique probe to show the existence of the nematic state in monolayer samples is the non-linear Hall effect [61], which vanishes for D_3 symmetry but becomes possible once it is broken. We believe our theory, in conjunction with new experiments, will finally serve to settle the symmetry of the CDW states in TiSe_2 .

Acknowledgements.— We are grateful to M. Ugeda, M. Gastiasoro, F. Flicker, J. van Wezel and M. Watson for interesting discussions on our work. D.M.S. is supported by an FPU predoctoral contract from Spanish Ministerio de Ciencia, Innovación y Universidades (MCIU) No. FPU19/03195. A.G.G. acknowledges financial support from the European Research Council (ERC) Consolidator grant under grant agreement No. 101042707 (TOPOMORPH). J.W.F.V. was supported by the National Science Foundation (NSF) Award No. DMR-2144352. F.J. acknowledges funding from the Spanish MCI/AEI/FEDER through grant PID2021-128760NB-I00.

[1] F. J. Di Salvo, D. Moncton, and J. Waszczak, Electronic properties and superlattice formation in the semimetal TiSe_2 , *Phys. Rev. B* **14**, 4321 (1976).
 [2] K. Rossnagel, On the origin of charge-density waves in select layered transition-metal dichalcogenides, *J. Phys.: Cond. Matt.* **23**, 213001 (2011).

[3] F. Weber, S. Rosenkranz, J.-P. Castellán, R. Osborn, G. Karapetrov, R. Hott, R. Heid, K.-P. Bohnen, and A. Alatas, Electron-phonon coupling and the soft phonon mode in TiSe_2 , *Phys. Rev. Lett.* **107**, 266401 (2011).
 [4] M. Calandra and F. Mauri, Charge-density wave and superconducting dome in TiSe_2 from electron-phonon interaction, *Phys. Rev. Lett.* **106**, 196406 (2011).
 [5] C. Monney, H. Cercellier, F. Clerc, C. Battaglia, E. F. Schwier, C. Didiot, M. G. Garnier, H. Beck, P. Aebi, H. Berger, L. Forró, and L. Patthey, Spontaneous exciton condensation in 1T-TiSe_2 : BCS-like approach, *Phys. Rev. B* **79**, 045116 (2009).
 [6] A. Kogar, M. S. Rak, S. Vig, A. A. Husain, F. Flicker, Y. I. Joe, L. Venema, G. J. MacDougall, T. C. Chiang, E. Fradkin, *et al.*, Signatures of exciton condensation in a transition metal dichalcogenide, *Science* **358**, 1314 (2017).
 [7] J. van Wezel, P. Nahai-Williamson, and S. S. Saxena, An alternative interpretation of recent arpes measurements on TiSe_2 , *Europhys. Lett.* **89**, 47004 (2010).
 [8] J. van Wezel, P. Nahai-Williamson, and S. S. Saxena, Exciton-phonon-driven charge density wave in TiSe_2 , *Phys. Rev. B* **81**, 165109 (2010).
 [9] M. Porer, U. Leierseder, J.-M. Ménard, H. Dachraoui, L. Mouchliadis, I. E. Perakis, U. Heinzmann, J. Demsar, K. Rossnagel, and R. Huber, Non-thermal separation of electronic and structural orders in a persisting charge density wave, *Nature Materials* **13**, 857 (2014).
 [10] C. Monney, M. Puppín, C. W. Nicholson, M. Hoesch, R. T. Chapman, E. Springate, H. Berger, A. Magrez, C. Cacho, R. Ernstorfer, and M. Wolf, Revealing the role of electrons and phonons in the ultrafast recovery of charge density wave correlations in 1T-TiSe_2 , *Phys. Rev. B* **94**, 165165 (2016).
 [11] M. Holt, P. Zschack, H. Hong, M. Y. Chou, and T.-C. Chiang, X-ray studies of phonon softening in TiSe_2 , *Phys. Rev. Lett.* **86**, 3799 (2001).
 [12] J. Ishioka, Y. Liu, K. Shimatake, T. Kurosawa, K. Ichimura, Y. Toda, M. Oda, and S. Tanda, Chiral charge-density waves, *Phys. Rev. Lett.* **105**, 176401 (2010).
 [13] J. van Wezel, Chirality and orbital order in charge density waves, *Europhysics Letters* **96**, 67011 (2011).
 [14] J. Van Wezel, The chiral charge density wave transition in 1T-TiSe_2 , in *J. Phys.: Conf. Ser.*, Vol. 391 (IOP Publishing, 2012) p. 012167.
 [15] B. Zenker, H. Fehske, H. Beck, C. Monney, and A. R. Bishop, Chiral charge order in 1T-TiSe_2 : Importance of lattice degrees of freedom, *Phys. Rev. B* **88**, 075138 (2013).
 [16] M. Gradhand and J. van Wezel, Optical gyrotropy and the non-local hall effect in chiral charge-ordered TiSe_2 , *Phys. Rev. B* **92**, 041111 (2015).
 [17] J. Ishioka, T. Fujii, K. Katono, K. Ichimura, T. Kurosawa, M. Oda, and S. Tanda, Charge-parity symmetry observed through friedel oscillations in chiral charge-density waves, *Phys. Rev. B* **84**, 245125 (2011).
 [18] M. Iavarone, R. Di Capua, X. Zhang, M. Golalikhani, S. A. Moore, and G. Karapetrov, Evolution of the charge density wave state in Cu_xTiSe_2 , *Phys. Rev. B* **85**, 155103 (2012).
 [19] B. Hildebrand, T. Jaouen, M.-L. Mottas, G. Monney, C. Barreteau, E. Giannini, D. R. Bowler, and P. Aebi, Local real-space view of the achiral 1T-TiSe_2 $2 \times 2 \times 2$ charge density wave, *Phys. Rev. Lett.* **120**, 136404 (2018).
 [20] J.-P. Castellán, S. Rosenkranz, R. Osborn, K. Gray, X. Luo, U. Welp, G. Karapetrov, J. Ruff, J. van Wezel, *et al.*, Chiral phase transition in charge ordered 1T-TiSe_2 , *Physical Review Letters* **110**, 196404 (2013).
 [21] M.-K. Lin, J. A. Hlevyack, P. Chen, R.-Y. Liu, and T.-C. Chi-

- ang, Comment on “chiral phase transition in charge ordered 1T-TiSe₂”, *Phys. Rev. Lett.* **122**, 229701 (2019).
- [22] H. Ueda, M. Porer, J. R. L. Mardegan, S. Parchenko, N. Guring, F. Fabrizi, M. Ramakrishnan, L. Boie, M. J. Neugebauer, B. Burganov, M. Burian, S. L. Johnson, K. Rossnagel, and U. Staub, Correlation between electronic and structural orders in 1T-TiSe₂, *Phys. Rev. Research* **3**, L022003 (2021).
- [23] E. H. da Silva Neto, P. Aynajian, R. E. Baumbach, E. D. Bauer, J. Mydosh, S. Ono, and A. Yazdani, Detection of electronic nematicity using scanning tunneling microscopy, *Phys. Rev. B* **87**, 161117 (2013).
- [24] Y.-X. Jiang, J.-X. Yin, M. M. Denner, N. Shumiya, B. R. Ortiz, G. Xu, Z. Guguchia, J. He, M. S. Hossain, X. Liu, *et al.*, Unconventional chiral charge order in kagome superconductor KV₃Sb₅, *Nature Materials* **20**, 1353 (2021).
- [25] H. Li, H. Zhao, B. R. Ortiz, T. Park, M. Ye, L. Balents, Z. Wang, S. D. Wilson, and I. Zeljkovic, Rotation symmetry breaking in the normal state of a kagome superconductor KV₃Sb₅, *Nature Physics* **18**, 265 (2022).
- [26] L. Nie, K. Sun, W. Ma, D. Song, L. Zheng, Z. Liang, P. Wu, F. Yu, J. Li, M. Shan, *et al.*, Charge-density-wave-driven electronic nematicity in a kagome superconductor, *Nature* **604**, 59 (2022).
- [27] Y. Jiang, X. Lai, K. Watanabe, T. Taniguchi, K. Haule, J. Mao, and E. Y. Andrei, Charge order and broken rotational symmetry in magic-angle twisted bilayer graphene, *Nature* **573**, 91 (2019).
- [28] C. Rubio-Verdú, S. Turkel, Y. Song, L. Klebl, R. Samajdar, M. S. Scheurer, J. W. Venderbos, K. Watanabe, T. Taniguchi, H. Ochoa, *et al.*, Moiré nematic phase in twisted double bilayer graphene, *Nature Physics* **18**, 196 (2022).
- [29] D. J. Campbell, C. Eckberg, P. Y. Zavalij, H.-H. Kung, E. Razzoli, M. Michiardi, C. Jozwiak, A. Bostwick, E. Rotenberg, A. Damascelli, and J. Paglione, Intrinsic insulating ground state in transition metal dichalcogenide TiSe₂, *Phys. Rev. Materials* **3**, 053402 (2019).
- [30] M. D. Watson, A. M. Beales, and P. D. C. King, On the origin of the anomalous peak in the resistivity of TiSe₂, *Phys. Rev. B* **99**, 195142 (2019).
- [31] P. Knowles, B. Yang, T. Muramatsu, O. Moulding, J. Buhot, C. J. Sayers, E. Da Como, and S. Friedemann, Fermi surface reconstruction and electron dynamics at the charge-density-wave transition in TiSe₂, *Phys. Rev. Lett.* **124**, 167602 (2020).
- [32] A. Kogar, G. A. de la Pena, S. Lee, Y. Fang, S. X.-L. Sun, D. B. Lioi, G. Karapetrov, K. D. Finkelstein, J. P. C. Ruff, P. Abbamonte, and S. Rosenkranz, Observation of a charge density wave incommensuration near the superconducting dome in Cu_xTiSe₂, *Phys. Rev. Lett.* **118**, 027002 (2017).
- [33] S. Yan, D. Iai, E. Morosan, E. Fradkin, P. Abbamonte, and V. Madhavan, Influence of domain walls in the incommensurate charge density wave state of Cu intercalated 1T-TiSe₂, *Phys. Rev. Lett.* **118**, 106405 (2017).
- [34] E. Morosan, H. W. Zandbergen, B. Dennis, J. Bos, Y. Onose, T. Klimczuk, A. Ramirez, N. Ong, and R. J. Cava, Superconductivity in Cu_xTiSe₂, *Nat. Phys.* **2**, 544 (2006).
- [35] L. Li, E. O’Farrell, K. Loh, G. Eda, B. Özyilmaz, and A. C. Neto, Controlling many-body states by the electric-field effect in a two-dimensional material, *Nature* **529**, 185 (2015).
- [36] M. J. Wei, W. J. Lu, R. C. Xiao, H. Y. Lv, P. Tong, W. H. Song, and Y. P. Sun, Manipulating charge density wave order in monolayer 1T-TiSe₂ by strain and charge doping: A first-principles investigation, *Phys. Rev. B* **96**, 165404 (2017).
- [37] B. Guster, E. Canadell, M. Pruneda, and P. Ordejón, First principles analysis of the CDW instability of single-layer 1T-TiSe₂ and its evolution with charge carrier density, *2D Mater.* **5**, 025024 (2018).
- [38] C. Chen, B. Singh, H. Lin, and V. M. Pereira, Reproduction of the Charge Density Wave Phase Diagram in 1T-TiSe₂ Exposes its Excitonic Character, *Phys. Rev. Lett.* **121**, 226602 (2018).
- [39] C. Chen, L. Su, A. H. Castro Neto, and V. M. Pereira, Discommensuration-driven superconductivity in the charge density wave phases of transition-metal dichalcogenides, *Phys. Rev. B* **99**, 121108 (2019).
- [40] D. Novko, Z. Torbatian, and I. Lončarić, Electron correlations rule the phonon-driven instability in single-layer TiSe₂, *Phys. Rev. B* **106**, 245108 (2022).
- [41] A. Zunger and A. J. Freeman, Band structure and lattice instability of TiSe₂, *Phys. Rev. B* **17**, 1839 (1978).
- [42] J. C. E. Rasch, T. Stemmler, B. Müller, L. Dudy, and R. Manzke, 1T-TiSe₂: Semimetal or Semiconductor?, *Phys. Rev. Lett.* **101**, 237602 (2008).
- [43] M.-L. Mottas, T. Jaouen, B. Hildebrand, M. Rumo, F. Vanini, E. Razzoli, E. Giannini, C. Barreteau, D. R. Bowler, C. Monney, H. Beck, and P. Aebi, Semimetal-to-semiconductor transition and charge-density-wave suppression in 1T-TiSe_{2-x}S_x single crystals, *Phys. Rev. B* **99**, 155103 (2019).
- [44] M. D. Watson, O. J. Clark, F. Mazzola, I. Marković, V. Sunko, T. K. Kim, K. Rossnagel, and P. D. C. King, Orbital- and *k_z*-selective hybridization of *se 4p* and *ti 3d* states in the charge density wave phase of TiSe₂, *Phys. Rev. Lett.* **122**, 076404 (2019).
- [45] T. Jaouen, B. Hildebrand, M.-L. Mottas, M. Di Giovannantonio, P. Ruffieux, M. Rumo, C. W. Nicholson, E. Razzoli, C. Barreteau, A. Ubaldini, E. Giannini, F. Vanini, H. Beck, C. Monney, and P. Aebi, Phase separation in the vicinity of Fermi surface hot spots, *Phys. Rev. B* **100**, 075152 (2019).
- [46] M. D. Watson, A. Rajan, T. Antonelli, K. Underwood, I. Marković, F. Mazzola, O. J. Clark, G.-R. Siemann, D. Biswas, A. Hunter, *et al.*, Strong-coupling charge density wave in monolayer TiSe₂, *2D Materials* **8**, 015004 (2020).
- [47] G. Monney, C. Monney, B. Hildebrand, P. Aebi, and H. Beck, Impact of Electron-Hole Correlations on the 1T-TiSe₂ Electronic Structure, *Phys. Rev. Lett.* **114**, 086402 (2015).
- [48] See Supplemental Material at XX for the symmetry analysis of the different ground states, the analytical solution of the critical doping for the transition to the 1Q stripe phase, and details on the effective tight-binding model.
- [49] S. Kolekar, M. Bonilla, H. C. Diaz, M. Hashimoto, D. Lu, and M. Batzill, Controlling the Charge Density Wave Transition in Monolayer TiSe₂: Substrate and Doping Effects, *Advanced Quantum Technologies* **1**, 1800070 (2018).
- [50] M. Hellgren, J. Baima, R. Bianco, M. Calandra, F. Mauri, and L. Wirtz, Critical Role of the Exchange Interaction for the Electronic Structure and Charge-Density-Wave Formation in TiSe₂, *Phys. Rev. Lett.* **119**, 176401 (2017).
- [51] B. Valenzuela and M. A. Vozmediano, Pomeranchuk instability in doped graphene, *New Journal of Physics* **10**, 113009 (2008).
- [52] M. L. Kiesel, C. Platt, and R. Thomale, Unconventional fermi surface instabilities in the kagome hubbard model, *Phys. Rev. Lett.* **110**, 126405 (2013).
- [53] G. Wu, H. X. Yang, L. Zhao, X. G. Luo, T. Wu, G. Y. Wang, and X. H. Chen, Transport properties of single-crystalline Cu_xTiSe₂ (0.015 ≤ *x* ≤ 0.110), *Phys. Rev. B* **76**, 024513 (2007).
- [54] A. M. Novello, M. Spera, A. Scarfato, A. Ubaldini, E. Giannini, D. R. Bowler, and C. Renner, Stripe and short range order in the charge density wave of 1T-Cu_xTiSe₂, *Phys. Rev. Lett.* **118**, 017002 (2017).
- [55] S.-Y. Xu, Q. Ma, Y. Gao, A. Kogar, A. Zong, A. M. M. Valdivia, T. H. Dinh, S.-M. Huang, B. Singh, C.-H. Hsu, *et al.*, Spontaneous gyrotropic electronic order in a transition-metal

- dichalcogenide, *Nature* **578**, 545 (2020).
- [56] H. Jog, L. Harnagea, D. Rout, T. Taniguchi, K. Watanabe, E. J. Mele, and R. Agarwal, [Optically induced symmetry breaking due to nonequilibrium steady state formation in charge density wave material 1T-TiSe₂](#) (2023), arXiv:2304.13170.
- [57] D. Wickramaratne, S. Subedi, D. H. Torchinsky, G. Karapetrov, and I. I. Mazin, Photoinduced chiral charge density wave in TiSe₂, *Phys. Rev. B* **105**, 054102 (2022).
- [58] A. Subedi, Trigonal-to-monoclinic structural transition in TiSe₂ due to a combined condensation of $q = (\frac{1}{2}, 0, 0)$ and $(\frac{1}{2}, 0, \frac{1}{2})$ phonon instabilities, *Phys. Rev. Mater.* **6**, 014602 (2022).
- [59] M. Nunex-Regueiro, Uniaxial stress-induced resistivity anisotropy in TiSe₂ below 200K, *J. Phys. C: Solid State Phys.* **16**, L1061 (1983).
- [60] G. K. Scott, K. K. Bardhan, and J. C. Irwin, Raman scattering from the orthorhombic charge-density-wave state of 2H-TaSe₂, *Phys. Rev. Lett.* **50**, 771 (1983).
- [61] I. Sodemann and L. Fu, Quantum nonlinear hall effect induced by berry curvature dipole in time-reversal invariant materials, *Phys. Rev. Lett.* **115**, 216806 (2015).
- [62] M. I. Aroyo, J. M. Perez-Mato, D. Orobengoa, and E. Tasci, Crystallography online: Bilbao Crystallographic Server, *Bulg. Chem. Commun.* **43**, 183 (2011).
- [63] J. W. F. Venderbos, Symmetry analysis of translational symmetry broken density waves: Application to hexagonal lattices in two dimensions, *Phys. Rev. B* **93**, 115107 (2016).
- [64] J. W. F. Venderbos, Multi-Q hexagonal spin density waves and dynamically generated spin-orbit coupling: Time-reversal invariant analog of the chiral spin density wave, *Phys. Rev. B* **93**, 115108 (2016).
- [65] H. Cercellier, C. Monney, F. Clerc, C. Battaglia, L. Despont, M. G. Garnier, H. Beck, P. Aebi, L. Patthey, H. Berger, and L. Forró, Evidence for an Excitonic Insulator Phase in 1T-TiSe₂, *Phys. Rev. Lett.* **99**, 146403 (2007).
- [66] C. Monney, E. F. Schwier, M. G. Garnier, C. Battaglia, N. Mariotti, C. Didiot, H. Cercellier, J. Marcus, H. Berger, A. N. Titov, H. Beck, and P. Aebi, Dramatic effective mass reduction driven by strong electronic correlations, [arXiv:0912.5283 \[cond-mat\]](#) (2009), arXiv: 0912.5283.
- [67] R. Ganesh, G. Baskaran, J. van den Brink, and D. V. Efremov, Theoretical Prediction of a Time-Reversal Broken Chiral Superconducting Phase Driven by Electronic Correlations in a Single TiSe₂ Layer, *Phys. Rev. Lett.* **113**, 177001 (2014).
- [68] J. S. Zhou, L. Monacelli, R. Bianco, I. Errea, F. Mauri, and M. Calandra, Anharmonicity and Doping Melt the Charge Density Wave in Single-Layer TiSe₂, *Nano Lett.* **20**, 4809 (2020).
- [69] L. J. Li, W. J. Zhao, B. Liu, T. H. Ren, G. Eda, and K. P. Loh, Enhancing charge-density-wave order in 1T-TiSe₂ nanosheet by encapsulation with hexagonal boron nitride, *Appl. Phys. Lett.* **109**, 141902 (2016).
- [70] S. Kos, A. J. Millis, and A. I. Larkin, Gaussian fluctuation corrections to the BCS mean-field gap amplitude at zero temperature, *Phys. Rev. B* **70**, 214531 (2004).
- [71] W. L. McMillan, Landau theory of charge-density waves in transition-metal dichalcogenides, *Phys. Rev. B* **12**, 1187 (1975).
- [72] W. L. McMillan, Theory of discommensurations and the commensurate-incommensurate charge-density-wave phase transition, *Phys. Rev. B* **14**, 1496 (1976).

Supplemental Material: Nematic and stripe orders within the charge density wave state of doped TiSe₂

CONTENTS

References	5
A. Group theory, character tables and representation matrices	8
B. Symmetries of the different ground states	9
C. k.p model: analytical solution for the 3Q-1Q critical doping x_{1Q}	10
D. Tight-binding model and mean-field theory	12
1. Tight binding and model parameters	12
2. Mean-field theory: order parameters	14
3. Mean-field theory: calculation details	15
4. Additional $T - x$ phase diagrams	15

Appendix A: Group theory, character tables and representation matrices

The normal state of TiSe₂ has the symmorphic space group $P\bar{3}m1$ (#164), with point group D_{3d} . We will only consider the symmetry groups without spin. Its generators are $\{C_{3z}, C_{2x}, i\}$, with the center located in a Ti site. Its irreducible representations (irreps) are $\{A_{1g} \equiv \Gamma_1^+, A_{2g} \equiv \Gamma_2^+, E_g \equiv \Gamma_3^+, A_{1u} \equiv \Gamma_1^-, A_{2u} \equiv \Gamma_2^-, E_u \equiv \Gamma_3^-\}$ (see [62] for the character table). The subindex 1/2 in the A irreps indicates the parity under C_{2x} , and the subindex g/u or the superindex \pm refers to the parity under the intralayer inversion i .

The commensurate CDW has wavevector L in the bulk and M in the monolayer. Their little cogroup is C_{2h} . With the choice of the three $Q = \Gamma L, \Gamma M$ of Fig. 1 of the main text, $\mathbf{Q}_1 = (0, \frac{2\pi}{\sqrt{3}}, Q_z)$, $\mathbf{Q}_2 = (-\frac{\sqrt{3}}{2} \frac{2\pi}{\sqrt{3}}, -\frac{1}{2} \frac{2\pi}{\sqrt{3}}, Q_z)$, $\mathbf{Q}_3 = (\frac{\sqrt{3}}{2} \frac{2\pi}{\sqrt{3}}, -\frac{1}{2} \frac{2\pi}{\sqrt{3}}, Q_z)$, where $Q_z = \pi, 0$, the little cogroup of \mathbf{Q}_1 has generators $\{C_{2x}, i\}$. Their irreps are $\{Q_{1/2}^\pm\}$, which are all one-dimensional. Therefore, since there are three symmetry-equivalent Q points in the star, the order parameters with wavevector Q are three-dimensional.

A convenient approach to deal with the symmetry classification of $Q = \Gamma L, \Gamma M$ instabilities is the so-called extended point group [63, 64], where the translations that are broken by the CDW are included in the point group. Effectively one determines the symmetry group of the $2 \times 2(\times 2)$ supercell, and classifies the observables according to the irreps of this extended point group.

For the monolayer, where $Q = \Gamma M$, we perform group multiplication of the original point group D_{3d} with the group $\{E, t_1, t_2, t_3\}$, where t_1 represents the translation by $\mathbf{a}_1 = a(1, 0)$, t_2 by $\mathbf{a}_2 - \mathbf{a}_1 = a(-\frac{1}{2}, \frac{\sqrt{3}}{2})$, and t_3 by $-\mathbf{a}_2 = a(-\frac{1}{2}, -\frac{\sqrt{3}}{2})$. Due to the imposed translational symmetry with a 2×2 unit cell, the group multiplication rules are $t_i t_i = E$ and $t_i t_j = t_k$, with $i \neq j \neq k$. The extended point group in the monolayer, $D_{3d}^{(M)} = D_{3d} \wedge \{E, t_1, t_2, t_3\}$, is isomorphic to the cubic point group O_h . The generators of $D_{3d}^{(M)}$ are $\{C_{3z}, C_{2x}, i, t_1, t_2\}$, which are related to the generators $\{C_{3[111]}, C_{2[1-10]}, i, C_{2[001]}, C_{2[100]}\}$ of O_h via the isomorphism. The character table of $D_3^{(M)}$ (from which $D_{3d}^{(M)}$ is obtained by the direct product with the intralayer inversion i) and its correspondence with the point group O is shown in table I. The classes are $3t = \{t_1, t_2, t_3\}$, $6C_2 = \{C_{2l}, t_l C_{2l}\}$ (C_2 rotations and products of translations along axis l times C_2 rotations with the same axis l), $8C_3 = \{C_{3z}^\pm, t_l C_{3z}^\pm\}$, and $6tC_2 = \{t_l C_{2m}\}$ (products of translations along axis l times C_2 rotations with different axis m). The representation matrices of the generators of $D_3^{(M)}$ are shown in table II.

In the bulk, $Q = \Gamma L$, and the extended point group $D_{3d}^{(L)}$ is the direct product of $D_{3d}^{(M)}$ with the interlayer inversion symmetry I , with center in the midpoint between two Ti sites in adjacent layers, which commutes with all the other symmetry operations. Therefore, the irreps just carry an additional label indicating the parity under this interlayer inversion.

The character table and the explicit representation matrices allow us to build the symmetry constrained $\mathbf{k} \cdot \mathbf{p}$ Hamiltonian and its coupling to any order parameter. To do this, we remind that the momentum transforms as an E_u irrep $\{k_x, k_y\}$, the fermionic states transform as $M_1^+ \{d_1, d_2, d_3\}$ for the conduction bands and as $\Gamma_3^- \{p_x, p_y\}$ for the valence bands, and the order parameter $\bar{\Delta} = (\Delta_1, \Delta_2, \Delta_3)$ transforms as M_1^- . By multiplying irreps as desired and demanding that the total Hamiltonian be a scalar Γ_1^+ , all terms in the main text can be derived.

	$1E$	$3t(\equiv 3C_{2[100]})$	$6C_2(\equiv 6C_{2[1-10]})$	$8C_3$	$6tC_2(\equiv 6C_4)$
$\Gamma_1(\equiv A_1)$	1	1	1	1	1
$\Gamma_2(\equiv A_2)$	1	1	-1	1	-1
$\Gamma_3(\equiv E)$	2	2	0	-1	0
$M_1(\equiv T_2)$	3	-1	1	0	-1
$M_2(\equiv T_1)$	3	-1	-1	0	1

Table I. Character table of the extended point group $D_3^{(M)}$, and one-to-one correspondence with the cubic point group O .

	t_1	t_2	C_{3z}	C_{2x}
Γ_1	1	1	1	1
Γ_2	1	1	1	-1
Γ_3	$\begin{pmatrix} 1 & 0 \\ 0 & 1 \end{pmatrix}$	$\begin{pmatrix} 1 & 0 \\ 0 & 1 \end{pmatrix}$	$\begin{pmatrix} -\frac{1}{2} & -\frac{\sqrt{3}}{2} \\ \frac{\sqrt{3}}{2} & -\frac{1}{2} \end{pmatrix}$	$\begin{pmatrix} 1 & 0 \\ 0 & -1 \end{pmatrix}$
M_1	$\begin{pmatrix} 1 & 0 & 0 \\ 0 & -1 & 0 \\ 0 & 0 & -1 \end{pmatrix}$	$\begin{pmatrix} -1 & 0 & 0 \\ 0 & 1 & 0 \\ 0 & 0 & -1 \end{pmatrix}$	$\begin{pmatrix} 0 & 0 & 1 \\ 1 & 0 & 0 \\ 0 & 1 & 0 \end{pmatrix}$	$\begin{pmatrix} 1 & 0 & 0 \\ 0 & 0 & 1 \\ 0 & 1 & 0 \end{pmatrix}$
M_2	$\begin{pmatrix} 1 & 0 & 0 \\ 0 & -1 & 0 \\ 0 & 0 & -1 \end{pmatrix}$	$\begin{pmatrix} -1 & 0 & 0 \\ 0 & 1 & 0 \\ 0 & 0 & -1 \end{pmatrix}$	$\begin{pmatrix} 0 & 0 & 1 \\ 1 & 0 & 0 \\ 0 & 1 & 0 \end{pmatrix}$	$\begin{pmatrix} -1 & 0 & 0 \\ 0 & 0 & -1 \\ 0 & -1 & 0 \end{pmatrix}$

Table II. Representation matrices of the generators of the extended point group $D_3^{(M)}$.

Appendix B: Symmetries of the different ground states

The space group of the high temperature phase of TiSe_2 is $P\bar{3}m1$ (# 164, point group D_{3d}). For the monolayer, the order parameter $\vec{\Delta}$ transforms as M_1^- . The symmetry groups of the possible ground states for an M_1^- instability are shown in table III. While all components of the the M_1^- order parameter $\vec{\Delta}$ are odd under inversion with respect to the Ti sites, there is another inversion center on the bond connecting Ti sites. Both $\vec{\Delta} = (\Delta, 0, 0)$ and $\vec{\Delta} = (0, \Delta, \Delta)$ preserve at least one such inversion centers, so they are non chiral. States $\vec{\Delta} = (\Delta, \Delta, \Delta)$ and $\vec{\Delta} = (\Delta_1, \Delta_2, \Delta_2)$ however do break all inversion centers in the monolayer and they are chiral.

$\vec{\Delta}$	SG	PG
(Δ, Δ, Δ)	P321 (#149)	D_3
$(\Delta, 0, 0)$	C2/c (#15)	C_{2h}
$(0, \Delta, \Delta)$	C2/m (#12)	C_{2h}
$(\Delta_1, \Delta_2, \Delta_2)$	C2 (#5)	C_2
$(\Delta_1, \Delta_2, \Delta_3)$	P1 (#1)	1

Table III. Symmetry groups of the possible ordered phases in monolayer TiSe_2 .

In the bulk, the order parameter $\vec{\Delta}$ transforms as L_1^- and all ordered phases are achiral, since an interlayer inversion symmetry is always preserved. Chiral structures could be obtained with an M_1^- order parameter, which is not the leading bulk instability [57].

Appendix C: k.p model: analytical solution for the 3Q-1Q critical doping x_{1Q}

The existence of a critical doping x_{1Q} above which a 1Q solution for $\vec{\Delta}$ is obtained can be shown analytically in the $\mathbf{k} \cdot \mathbf{p}$ model in the simplified case where $b_p = b_d = 0$.

Consider a generic state $\vec{\Delta} = (\Delta_1, \Delta_2, \Delta_3)$ parametrized as $\vec{\Delta} = |\vec{\Delta}|[\cos(\theta), \sin(\theta)\cos(\varphi), \sin(\theta)\sin(\varphi)]$ with $|\vec{\Delta}| = \sqrt{\Delta_1^2 + \Delta_2^2 + \Delta_3^2}$, $\theta \in [0, \pi]$, and $\varphi \in [0, 2\pi]$. The energies of the bands for $b_p = b_d = 0$ are:

$$\varepsilon_{c0}(\mathbf{k}) = \frac{E_g}{2} + a_d k^2, \quad (C1)$$

$$\begin{aligned} \varepsilon_{c\pm}(\mathbf{k}) &= \frac{1}{2} \left[(a_d + a_p)k^2 + \sqrt{[E_g + (a_d - a_p)k^2]^2 + \frac{4}{3} \left(|\vec{\Delta}|^2 \pm \sqrt{\frac{3}{2}(\Delta_1^4 + \Delta_2^4 + \Delta_3^4) - \frac{1}{2}|\vec{\Delta}|^4} \right)} \right] = \\ &= \frac{1}{2} \left[(a_d + a_p)k^2 + \sqrt{[E_g + (a_d - a_p)k^2]^2 + \frac{4}{3}|\vec{\Delta}|^2 f_{\pm}(\theta, \varphi)} \right], \end{aligned} \quad (C2)$$

$$\begin{aligned} \varepsilon_{v\pm}(\mathbf{k}) &= \frac{1}{2} \left[(a_d + a_p)k^2 - \sqrt{[E_g + (a_d - a_p)k^2]^2 + \frac{4}{3} \left(|\vec{\Delta}|^2 \pm \sqrt{\frac{3}{2}(\Delta_1^4 + \Delta_2^4 + \Delta_3^4) - \frac{1}{2}|\vec{\Delta}|^4} \right)} \right] = \\ &= \frac{1}{2} \left[(a_d + a_p)k^2 - \sqrt{[E_g + (a_d - a_p)k^2]^2 + \frac{4}{3}|\vec{\Delta}|^2 f_{\pm}(\theta, \varphi)} \right], \end{aligned} \quad (C3)$$

where $k = |\mathbf{k}|$ and we have defined $f_{\pm}(\theta, \varphi) = 1 \pm \sqrt{\frac{3}{2}(\cos^4(\theta) + \sin^4(\theta)\cos^4(\varphi) + \sin^4(\theta)\sin^4(\varphi)) - \frac{1}{2}}$. $\varepsilon_{v\pm}$ are the two valence bands, ε_{c0} is the lowest conduction band, which always remains uncoupled, and $\varepsilon_{c\pm}$ are the two highest conduction bands.

Note that the energies only depend on the direction of $\vec{\Delta}$ via the quartic invariant $(\Delta_1^4 + \Delta_2^4 + \Delta_3^4)$, which, for a given modulus $|\vec{\Delta}|$, is minimum for $\vec{\Delta} = \frac{|\vec{\Delta}|}{\sqrt{3}}(1, 1, 1)$, and maximum for $\vec{\Delta} = |\vec{\Delta}|(1, 0, 0)$. Let us assume that the CDW phase displays a gap between valence and conduction bands so that the valence bands are fully filled at stoichiometry $x = 0$ (for which $E_g > 0$ is a sufficient condition). Then the ground state in the undoped case $x = 0$ has to be either the 3Q C_3 -symmetric state $\vec{\Delta} = \frac{|\vec{\Delta}|}{\sqrt{3}}(1, 1, 1)$ or the 1Q stripe state $\vec{\Delta} = |\vec{\Delta}|(1, 0, 0)$. For the 3Q C_3 -symmetric state, two pairs of valence and conduction bands are repelled and remain degenerate:

$$\varepsilon_{c+}^{3Q}(\mathbf{k}) = \varepsilon_{c-}^{3Q}(\mathbf{k}) = \varepsilon_c^{3Q}(\mathbf{k}) = \frac{1}{2} \left[(a_d + a_p)k^2 + \sqrt{[E_g + (a_d - a_p)k^2]^2 + \frac{4}{3}|\vec{\Delta}|^2} \right], \quad (C4)$$

$$\varepsilon_{v+}^{3Q}(\mathbf{k}) = \varepsilon_{v-}^{3Q}(\mathbf{k}) = \varepsilon_v^{3Q}(\mathbf{k}) = \frac{1}{2} \left[(a_d + a_p)k^2 - \sqrt{[E_g + (a_d - a_p)k^2]^2 + \frac{4}{3}|\vec{\Delta}|^2} \right], \quad (C5)$$

while for the 1Q stripe state, only one pair of valence and conduction bands is repelled:

$$\varepsilon_{c+}^{1Q}(\mathbf{k}) = \frac{1}{2} \left[(a_d + a_p)k^2 + \sqrt{[E_g + (a_d - a_p)k^2]^2 + \frac{8}{3}|\vec{\Delta}|^2} \right], \quad (C6)$$

$$\varepsilon_{c-}^{1Q}(\mathbf{k}) = \varepsilon_{c0}(\mathbf{k}), \quad (C7)$$

$$\varepsilon_{v+}^{1Q}(\mathbf{k}) = \frac{1}{2} \left[(a_d + a_p)k^2 - \sqrt{[E_g + (a_d - a_p)k^2]^2 + \frac{8}{3}|\vec{\Delta}|^2} \right], \quad (C8)$$

$$\varepsilon_{v-}^{1Q}(\mathbf{k}) = -\frac{E_g}{2} + a_p k^2, \quad (C9)$$

In order to determine the ground state, let us compute the difference in total energy density at zero temperature $\delta E = E - E^{3Q}$

between a generic state $\vec{\Delta} = (\Delta_1, \Delta_2, \Delta_3)$ and the $\vec{\Delta} = \frac{|\vec{\Delta}|}{\sqrt{3}}(1, 1, 1)$ phase. At stoichiometry $x = 0$,

$$\begin{aligned} \delta E(x=0) &= \int \frac{d^2k}{(2\pi)^2} [\varepsilon_{v+}(\mathbf{k}) + \varepsilon_{v-}(\mathbf{k}) - 2\varepsilon_v^{3Q}(\mathbf{k})] = \\ &= \frac{1}{8\pi(a_d - a_p)} \left\{ \frac{E_g}{2} \left(\sqrt{E_g^2 + \frac{4}{3}|\vec{\Delta}|^2} f_+(\theta, \varphi) + \sqrt{E_g^2 + \frac{4}{3}|\vec{\Delta}|^2} f_-(\theta, \varphi) - 2\sqrt{E_g^2 + \frac{4}{3}|\vec{\Delta}|^2} \right) + \right. \\ &\quad \left. + \frac{4}{3}|\vec{\Delta}|^2 \left[\log \left(-E_g + \sqrt{E_g^2 + \frac{4}{3}|\vec{\Delta}|^2} \right) - \frac{1}{2}f_+(\theta, \varphi) \log \left(\frac{-E_g + \sqrt{E_g^2 + \frac{4}{3}|\vec{\Delta}|^2} f_+(\theta, \varphi)}{f_+(\theta, \varphi)} \right) - \right. \right. \\ &\quad \left. \left. - \frac{1}{2}f_-(\theta, \varphi) \log \left(\frac{-E_g + \sqrt{E_g^2 + \frac{4}{3}|\vec{\Delta}|^2} f_-(\theta, \varphi)}{f_-(\theta, \varphi)} \right) \right] \right\}. \end{aligned} \quad (\text{C10})$$

$\delta E(x=0)$ is always a non-negative quantity, and it is equal to zero only if $\vec{\Delta} = \frac{|\vec{\Delta}|}{\sqrt{3}}(1, 1, 1)$, when $f_{\pm}(\theta, \varphi) = 1$. Therefore, the ground state at charge neutrality is the $3Q$ C_3 -symmetric state, and the $1Q$ stripe state has the highest energy:

$$\delta E^{1Q}(x=0) = \frac{1}{8\pi(a_d - a_p)} \left[\frac{E_g}{2} \left(\sqrt{E_g^2 + \frac{8}{3}|\vec{\Delta}|^2} + E_g - 2\sqrt{E_g^2 + \frac{4}{3}|\vec{\Delta}|^2} \right) + \frac{4}{3}|\vec{\Delta}|^2 \log \left(2 \frac{-E_g + \sqrt{E_g^2 + \frac{4}{3}|\vec{\Delta}|^2}}{-E_g + \sqrt{E_g^2 + \frac{8}{3}|\vec{\Delta}|^2}} \right) \right]. \quad (\text{C11})$$

In the limit $E_g \rightarrow 0$ we have simply $\delta E(x=0) = \frac{|\vec{\Delta}|^2}{24\pi(a_d - a_p)} [f_+ \log(f_+) + f_- \log(f_-)]$, and $\delta E^{1Q}(x=0) = \frac{|\vec{\Delta}|^2}{12\pi(a_d - a_p)} \log 2$.

Let us note that $\delta E(x=0)$ decreases with increasing E_g for fixed $|\vec{\Delta}|$.

Now consider doping a small carrier density $n = x/V_{\text{unit cell}}$ such that only the lowest conduction band ε_{c0} is populated. This assumption holds in the majority of the $\mathbf{k} \cdot \mathbf{p}$ phase diagrams of Figs. 2(c,d) (except for some regions in the case of large negative gap and small ellipticity, as explained in the main text). This assumption is also verified in all the self-consistent mean-field calculations. Except for the $1Q$ phase, the lowest conduction band is non-degenerate and equal for all $|\vec{\Delta}|$, so that the total energy difference $\delta E(x)$ remains the same as $\delta E(x=0)$.

However, the $1Q$ stripe phase displays a doubly-degenerate lowest conduction band. In this case, for a given carrier density n , the chemical potential is lower for the $1Q$ state than for the $3Q$ one, which allows the possibility of a transition to the $1Q$ phase at a critical doping, as we show below. The lowest conduction band is uncoupled by the order parameter, and thus remains parabolic with constant DOS $1/(4\pi a_d)$. The chemical potential is set by the carrier density:

$$n = \int_0^{\mu^{3Q}} d\varepsilon \frac{1}{4\pi a_d} \theta(\varepsilon - E_g/2) = \frac{\mu^{3Q} - E_g/2}{4\pi a_d} \quad (\text{C12})$$

$$n = \int_0^{\mu^{1Q}} d\varepsilon \frac{2}{4\pi a_d} \theta(\varepsilon - E_g/2) = \frac{\mu^{1Q} - E_g/2}{2\pi a_d} \quad (\text{C13})$$

$$(\text{C14})$$

And the total energy density difference is

$$\delta E^{1Q}(x) - \delta E^{1Q}(x=0) = \int_0^{\mu^{1Q}} d\varepsilon \frac{\varepsilon}{2\pi a_d} \theta(\varepsilon - E_g/2) - \int_0^{\mu^{3Q}} d\varepsilon \frac{\varepsilon}{4\pi a_d} \theta(\varepsilon - E_g/2) = \quad (\text{C15})$$

$$= \frac{1}{8\pi a_d} [2(2\pi a_d n)^2 - (4\pi a_d n)^2] = -\pi a_d n^2 \quad (\text{C16})$$

The transition to the $1Q$ state occurs at the x_{1Q} such that $\delta E^{1Q}(x_{1Q}) = 0$, so

$$n_{1Q} = 2\sqrt{\frac{\delta E^{1Q}(x=0)}{\pi a_d}}, \quad (\text{C17})$$

where we have added a factor 2 to take into account the spin degeneracy. In the limit $E_g \rightarrow 0$, we have $n_{1Q} = \frac{|\vec{\Delta}|}{\pi} \sqrt{\frac{\log 2}{3a_d(a_d - a_p)}}$.

We can estimate x_{1Q} from this calculation taking $a_p = -0.89\hbar^2/m_e$ and $a_d = 0.27\hbar^2/m_e$, with m_e the electron mass, which reproduce the same normal-state DOS as the realistic values $a_p = -0.95\hbar^2/m_e$, $b_p = -0.24\hbar^2/m_e$, $a_d = 0.54\hbar^2/m_e$ and $b_d = 0.46\hbar^2/m_e$ used in our effective tight-binding model. From the ARPES experiment on monolayer TiSe₂ of Ref. [46], where the normal-state gap is $E_g \sim 80\text{meV}$ and the low-temperature gap is $E_g/2 + \sqrt{E_g^2 + 4|\vec{\Delta}|^2/3} \sim 180\text{meV}$, one obtains an order parameter $|\vec{\Delta}| \sim 230\text{meV}$ in the low-doping case. Using these numerical values, we can estimate the critical doping for the transition from the $3Q$ to the $1Q$ states to be $x_{1Q} \sim 0.07e/f.u.$. Despite neglecting b_p and b_d , this value is of the order of magnitude of that obtained in the self-consistent mean-field calculations. The quantitative agreement is even better for a smaller $|\vec{\Delta}|$, which accounts for its decrease with increasing doping. The numerical results for x_{1Q} for $E_g > 0$ and nonzero b_p and b_d are displayed in Fig. 2(c), which demonstrates that if the CDW survives at high enough doping, a $1Q$ phase universally appears for any ellipticity and gap.

Appendix D: Tight-binding model and mean-field theory

Here we describe the effective tight-binding model, the choice of its parameters, and the details of the self-consistent mean-field calculations.

1. Tight binding and model parameters

The realistic tight-binding model of TiSe₂ would consist of at least 7 orbitals per unit cell: the four $\{p_x, p_y\}$ orbitals from the two Se atoms, which transform as E_u representations, and the t_{2g} triplet of d orbitals $\{d_{xy}, d_{yz}, d_{zx}\}$ from the Ti (the approximately cubic environment of Ti makes it useful to refer to these orbitals as t_{2g} even though they are actually split in a singlet A_{1g} and a doublet E_g because the overall crystal symmetry is trigonal). In 2D and in the absence of SOC, the low-energy physics is dominated by two degenerate hole pockets at Γ coming from the Se- p orbitals which transform as the Γ_3^- representation, and three electron pockets at the M points coming from the Ti- d orbitals which transform according to the M_1^+ representation.

Here, we have considered instead an effective tight-binding model with the same space group $P\bar{3}m1$ (SG 164, PG D_{3d}) which reproduces the band dispersion and eigenstate symmetry near the Fermi level with 3 orbitals per unit cell (formally, the model also has a m_z symmetry, but it plays no role because all orbitals are located at $z = 0$). The 3 orbitals are located at the center of a triangular lattice. Two orbitals transform as E_u , and mainly compose the valence bands, so they will be denoted as $\{p_x, p_y\}$. The other orbital is totally symmetric (A_{1g}), and mainly composes the conduction band, so it will be denoted as d_{z^2} . The non-interacting model has 8 parameters: onsite energies ε_p and ε_d , hoppings up to third nearest neighbours $t_{dd}^{(n)}$ for the d_{z^2} orbital, σ and π nearest-neighbour hoppings $t_{pp\sigma}$ and $t_{pp\pi}$ for the p orbitals, and nearest-neighbour hopping t_{dp} coupling the d and p orbitals. The non-interacting Hamiltonian is given by Eq. (6) of the main text. In this Hamiltonian we have neglected SOC. While this can quantitatively change the critical temperature and related quantities, we expect that the qualitative picture remains the same [50].

We choose the Hamiltonian parameters by solving for the the non-interacting gap E_g , the masses m_{v1}, m_{v2} of the two valence bands at Γ , the masses m_{cx}, m_{cy} of the conduction bands at M perpendicular and parallel to the ΓM direction, and the energy $\varepsilon_{c\Gamma}$ of the conduction band at Γ . The resulting system of equations would be underconstrained, so we choose to leave t_{dp} as a free parameter. Since the valence bands are of p character while the conduction bands are d character, t_{dp} only affects the band curvatures to second order with an energy denominator dominated by $\varepsilon_d - \varepsilon_p$, so its influence on the bands is almost negligible. Nevertheless, we choose to keep it finite because it breaks the artificial $U(1)$ gauge symmetry representing the separate charge conservation in the conduction and valence bands. The subtle role of t_{dp} in selecting a mean field solution is further explained below in Sec. D 2.

The gap, the masses and $\varepsilon_{c\Gamma}$ depend on the hoppings as:

$$\begin{aligned}
E_g &= \varepsilon_d - \varepsilon_p - \left[2t_{dd}^{(1)} + 2t_{dd}^{(2)} - 6t_{dd}^{(3)} - 3t_{pp\sigma} + 3t_{pp\pi} \right] \\
\varepsilon_{c\Gamma} &= \varepsilon_d + 6 \left[t_{dd}^{(1)} + t_{dd}^{(2)} + t_{dd}^{(3)} \right] \\
\tilde{m}_{v1}^{-1} &= \frac{3}{4} [t_{pp\sigma} - 3t_{pp\pi}] \\
\tilde{m}_{v2}^{-1} &= -\frac{3}{4} \left[-3t_{pp\sigma} + t_{pp\pi} + \frac{24t_{dp}^2}{\varepsilon_d - \varepsilon_p + 3 \left(2t_{dd}^{(1)} + 2t_{dd}^{(2)} + 2t_{dd}^{(3)} + t_{pp\sigma} - t_{pp\pi} \right)} \right] \\
\tilde{m}_{cy}^{-1} &= 3 \left[t_{dd}^{(1)} - t_{dd}^{(2)} - 4t_{dd}^{(3)} + \frac{6t_{dp}^2}{\varepsilon_d - \varepsilon_p - \left(2t_{dd}^{(1)} + 2t_{dd}^{(2)} - 6t_{dd}^{(3)} + 3t_{pp\sigma} + t_{pp\pi} \right)} \right] \\
\tilde{m}_{cx}^{-1} &= -t_{dd}^{(1)} + 9t_{dd}^{(2)} - 12t_{dd}^{(3)} + \frac{2t_{dp}^2}{\varepsilon_d - \varepsilon_p - \left(2t_{dd}^{(1)} + 2t_{dd}^{(2)} - 6t_{dd}^{(3)} - t_{pp\sigma} - 3t_{pp\pi} \right)}
\end{aligned} \tag{D1}$$

where we have defined $\tilde{m} = ma^2/\hbar^2$, where a is the lattice constant. Inverting these relationships, we find that the hoppings as a function of the gap, the masses, $\varepsilon_{c\Gamma}$ and t_{dp} can be expressed as:

$$\begin{aligned}
\varepsilon_d &= \frac{1}{256} \left(48\tilde{m}_{cx}^{-1} + 80\tilde{m}_{cy}^{-1} + \frac{288t_{dp}^2}{8\tilde{m}_{v1}^{-1} - 3E_g} - \frac{15(8\tilde{m}_{v2}^{-1} - 3E_g)(2\varepsilon_{c\Gamma} + E_g)^2}{(8\tilde{m}_{v2}^{-1} - 3E_g)(2\varepsilon_{c\Gamma} + E_g) + 288t_{dp}^2} + 70\varepsilon_{c\Gamma} + 123E_g \right) \\
\varepsilon_p &= \tilde{m}_{v1}^{-1} + \tilde{m}_{v2}^{-1} + \frac{36t_{dp}^2}{2\varepsilon_{c\Gamma} + E_g} - \frac{E_g}{2} \\
t_{dd}^{(1)} &= \frac{1}{256} \left(-16\tilde{m}_{cx}^{-1} + 16\tilde{m}_{cy}^{-1} + \frac{96t_{dp}^2}{3E_g - 8\tilde{m}_{v1}^{-1}} - \frac{3(8\tilde{m}_{v2}^{-1} - 3E_g)(2\varepsilon_{c\Gamma} + E_g)^2}{(8\tilde{m}_{v2}^{-1} - 3E_g)(2\varepsilon_{c\Gamma} + E_g) + 288t_{dp}^2} + 30\varepsilon_{c\Gamma} - 9E_g \right) \\
t_{pp\sigma} &= -\frac{\tilde{m}_{v1}^{-1}}{6} + \frac{\tilde{m}_{v2}^{-1}}{2} + \frac{18t_{dp}^2}{2\varepsilon_{c\Gamma} + E_g} \\
t_{pp\pi} &= -\frac{\tilde{m}_{v1}^{-1}}{2} + \frac{\tilde{m}_{v2}^{-1}}{6} + \frac{6t_{dp}^2}{2\varepsilon_{c\Gamma} + E_g} \\
t_{dd}^{(2)} &= \frac{1}{256} \left(16\tilde{m}_{cx}^{-1} - 16\tilde{m}_{cy}^{-1} + \frac{96t_{dp}^2}{8\tilde{m}_{v1}^{-1} - 3E_g} - \frac{3(3E_g - 8\tilde{m}_{v2}^{-1})(2\varepsilon_{c\Gamma} + E_g)^2}{(8\tilde{m}_{v2}^{-1} - 3E_g)(2\varepsilon_{c\Gamma} + E_g) + 288t_{dp}^2} + 2\varepsilon_{c\Gamma} - 7E_g \right) \\
t_{dd}^{(3)} &= \frac{1}{1536} \left[-48\tilde{m}_{cx}^{-1} - 80\tilde{m}_{cy}^{-1} + 3 \left(\frac{96t_{dp}^2}{3E_g - 8\tilde{m}_{v1}^{-1}} - \frac{5(3E_g - 8\tilde{m}_{v2}^{-1})(2\varepsilon_{c\Gamma} + E_g)^2}{(8\tilde{m}_{v2}^{-1} - 3E_g)(2\varepsilon_{c\Gamma} + E_g) + 288t_{dp}^2} - 2\varepsilon_{c\Gamma} - 9E_g \right) \right]
\end{aligned} \tag{D2}$$

Reference	Technique	m_{v1}/m_e	m_{v2}/m_e	m_{cy}/m_e	m_{cx}/m_e	m_{v2}/m_{v1}	$-m_{cy}/m_{v2}$	m_{cy}/m_{cx}
[49]	ARPES 2D	-0.7	-0.45	7.1	?	0.64	16	?
[5, 65]	ARPES 3D	?	-0.23	5.5	2.2	?	24	2.5
[66]	ARPES 3D	?	?	6	0.5	?	?	12
[38]	DFT 2D	?	-0.19	3.46	0.22	?	18	16
[37]	DFT 2D	-0.25	-0.15	5.6	0.4	0.60	37	14
[47]	DFT 3D	?	-0.22	4.3	0.29	?	20	15

Table IV. Values of the masses of the valence and conduction bands obtained in previous works.

Table IV shows different values of the masses of the bands extracted from previous works. Here, we choose the values of Ref. [49] based on ARPES measurements on monolayer TiSe₂: $m_{v1} = -0.7m_e$, $m_{v2} = (50/3)m_{v2} = -0.42m_e$, $m_{cy} = 10m_{v1} = 7m_e$, $m_{cx} = m_{cy}/14 = 0.5m_e$. Then, for gap $E_g = 0$ as in the inset of Fig. 4 of the main text, the hopping parameters

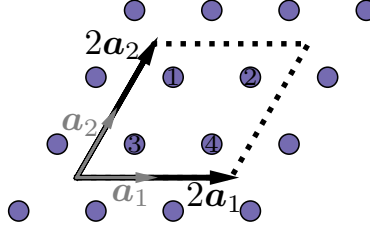


Figure S1. Triangular lattice of the effective tight-binding model with our choice of lattice vectors and supercell.

are $\varepsilon_d \simeq 0.329\text{eV}$, $\varepsilon_p \simeq -2.016\text{eV}$, $t_{dd}^{(1)} \simeq -0.017\text{eV}$, $t_{dd}^{(2)} \simeq 0.092\text{eV}$, $t_{dd}^{(3)} \simeq -0.030\text{eV}$, $t_{pp\sigma} \simeq -0.429\text{eV}$, $t_{pp\pi} \simeq 0.243\text{eV}$, and $t_{dp} \simeq 0.1\text{eV}$.

2. Mean-field theory: order parameters

By decoupling the Hamiltonian $H_0 + H_{\text{int}}$ of Eqs. (6),(7) of the main text in the onsite orbital order $\langle d_i^\dagger \mathbf{p}_i \rangle$ channel, which corresponds to the Fock channel of the V_{dp} interaction, the mean-field Hamiltonian in real-space becomes

$$H_{\text{MF}} = H_0 + V_{dp} \sum_{\langle ij \rangle} \left\{ \left[\langle d_i^\dagger \mathbf{p}_i \rangle^* \cdot (2\hat{\mathbf{r}}_{ij} \otimes \hat{\mathbf{r}}_{ij} - 1) \cdot \langle d_j^\dagger \mathbf{p}_j \rangle + \text{h.c.} \right] - \langle d_i^\dagger \mathbf{p}_i \rangle^* \cdot (2\hat{\mathbf{r}}_{ij} \otimes \hat{\mathbf{r}}_{ij} - 1) \cdot \langle d_j^\dagger \mathbf{p}_j \rangle \right\}, \quad (\text{D3})$$

with the expectation values taken in the mean-field ground state. We solve H_{MF} in a 2×2 supercell with superlattice vectors $2\mathbf{a}_i$, with $\mathbf{a}_1 = a(1, 0)$ and $\mathbf{a}_2 = a(\frac{1}{2}, \frac{\sqrt{3}}{2})$ and label the supercell sites by $j = 1, 2, 3, 4$ (see Fig. S1). Without loss of generality, we choose the origin of coordinates of a cell at $\mathbf{r}_1 = (0, 0)$, so $\mathbf{r}_2 = a(1, 0)$, $\mathbf{r}_3 = a(-1/2, -\sqrt{3}/2)$, and $\mathbf{r}_4 = a(1/2, -\sqrt{3}/2)$.

Let us classify according to symmetry the different terms entering the Hamiltonian. In the original unit cell, the onsite orbital orders $(d^\dagger p_x \pm \text{h.c.}, d^\dagger p_y \pm \text{h.c.})$ transform as TRS even and odd Γ_3^- , which correspond to the irrep. E_u .

Now, let us consider the symmetry classification in the 2×2 supercell. The orbital orders $d^\dagger p_\alpha$ transform as $\Gamma_3^- \oplus M_1^- \oplus M_2^-$, where the M_1^- and M_2^- are irreps of the little group of the M points that are even and odd under the C_2 symmetry, respectively. The symmetry adapted operators read

$$[d^\dagger p]_{\Gamma_3^-}^\alpha = \frac{1}{2} \sum_j d_j^\dagger p_{\alpha j}, \quad (\text{D4})$$

$$[d^\dagger p]_{M_1^-}^a = \frac{1}{2} \sum_j e^{i\mathbf{M}_a \cdot \mathbf{r}_j} d_j^\dagger p_j \times \hat{\mathbf{M}}_a, \quad (\text{D5})$$

$$[d^\dagger p]_{M_2^-}^a = \frac{1}{2} \sum_j e^{i\mathbf{M}_a \cdot \mathbf{r}_j} d_j^\dagger p_j \cdot \hat{\mathbf{M}}_a, \quad (\text{D6})$$

where the subindices label the irrep. according to which the operators transform, and the superindices $\alpha = 1, 2$ and $a = 1, 2, 3$ label the different components of the multidimensional irreps. We have defined $\hat{\mathbf{M}}_a = \frac{\mathbf{M}_a}{|\mathbf{M}_a|}$, and $\mathbf{v} \times \mathbf{w} = v_x w_y - v_y w_x$. We use the notation indicated in Fig. 1 of the main text: $\mathbf{M}_1 = \frac{2\pi}{\sqrt{3}a}(0, 1)$, $\mathbf{M}_2 = \frac{2\pi}{\sqrt{3}a}(-\frac{\sqrt{3}}{2}, -\frac{1}{2})$, $\mathbf{M}_3 = \frac{2\pi}{\sqrt{3}a}(\frac{\sqrt{3}}{2}, -\frac{1}{2})$. TRS even and odd operators can be obtained by adding or subtracting the Hermitian conjugate, respectively.

Using the previous symmetry-adapted operators and the mean-field interaction of Eq. (D3), let us construct the symmetry-adapted order parameter $\vec{\Delta}$. In the basis $\{d_1^\dagger p_{x1}, d_1^\dagger p_{y1}, d_2^\dagger p_{x2}, d_2^\dagger p_{y2}, d_3^\dagger p_{x3}, d_3^\dagger p_{y3}, d_4^\dagger p_{x4}, d_4^\dagger p_{y4}\}$, the $\langle d^\dagger p \rangle$ decoupling of the

interaction V_{dp} reads:

$$V_{dp}\langle d^\dagger p \rangle^* \cdot \begin{pmatrix} 0 & 0 & 1 & 0 & -\frac{1}{2} & \frac{\sqrt{3}}{2} & -\frac{1}{2} & -\frac{\sqrt{3}}{2} \\ 0 & 0 & 0 & -1 & \frac{\sqrt{3}}{2} & \frac{1}{2} & -\frac{\sqrt{3}}{2} & \frac{1}{2} \\ 1 & 0 & 0 & 0 & -\frac{1}{2} & -\frac{\sqrt{3}}{2} & -\frac{1}{2} & \frac{\sqrt{3}}{2} \\ 0 & -1 & 0 & 0 & -\frac{\sqrt{3}}{2} & \frac{1}{2} & \frac{\sqrt{3}}{2} & \frac{1}{2} \\ -\frac{1}{2} & \frac{\sqrt{3}}{2} & -\frac{1}{2} & -\frac{\sqrt{3}}{2} & 0 & 0 & 1 & 0 \\ \frac{\sqrt{3}}{2} & \frac{1}{2} & -\frac{\sqrt{3}}{2} & \frac{1}{2} & 0 & 0 & 0 & -1 \\ -\frac{1}{2} & -\frac{\sqrt{3}}{2} & -\frac{1}{2} & \frac{\sqrt{3}}{2} & 1 & 0 & 0 & 0 \\ -\frac{\sqrt{3}}{2} & \frac{1}{2} & \frac{\sqrt{3}}{2} & \frac{1}{2} & 0 & -1 & 0 & 0 \end{pmatrix} \cdot d^\dagger p + \text{h.c.} \quad (\text{D7})$$

Diagonalizing this matrix, we get eigenvalue $-2V_{dp}$ for the eigenvectors $[d^\dagger p]_{M_1^-}$, $+2V_{dp}$ for $[d^\dagger p]_{M_2^-}$, and 0 for $[d^\dagger p]_{\Gamma_3^-}$. Therefore, the $\vec{\Delta}$ order parameter transforming as TRS even M_1^- and coupling the d and p orbitals is

$$\vec{\Delta} = -V_{dp} \sum_j e^{iM_a \cdot r_j} \text{Re}\langle d_j^\dagger p_j \rangle \times \hat{M}_a. \quad (\text{D8})$$

Our mean-field decoupling allows for another three order parameters. One is the TRS odd M_1^- counterpart of $\vec{\Delta}$, which corresponds to taking the imaginary part instead of the real part in Eq. (D8). In the presence of separate charge conservation for p and d orbitals, the time-reversal even and odd M_1^- order parameters would be degenerate [67]. However, the presence of a small t_{dp} hopping breaks their degeneracy in favor of the real part $\vec{\Delta}$ in all cases. Indeed, the TRS odd M_1^- order parameter is identically zero in our calculations. The other two order parameters transform as TRS even and odd M_2^- , $\vec{\Psi}_\pm = +V_{dp} \sum_j \frac{1}{2} (e^{iM_a \cdot r_j} \langle d_j^\dagger p_j \rangle \cdot \hat{M}_a \pm \text{h.c.})$, and the interaction is repulsive for both. Therefore, our interacting tight-binding model only favors time-reversal even M_1^- instabilities, as required.

3. Mean-field theory: calculation details

We perform self-consistent mean-field calculations on the Hamiltonian of Eq. (D3). For that, we introduce a initial seed for the order parameters, and recompute them iteratively until convergence is reached, defined as $\sqrt{\sum |\langle c^\dagger c \rangle_{n+1} - \langle c^\dagger c \rangle_n|} < \epsilon_0$. Since we work in the canonical ensemble, in each iteration we set the chemical potential to keep the number of particles fixed.

In order to find the ground state which minimizes the free energy, we initialize the self-consistent loop with different seeds: $\vec{\Delta} = (\Delta, \Delta, \Delta)$, $\vec{\Delta} = (\Delta, 0, 0)$, $\vec{\Delta} = (0, \Delta, \Delta)$, and $\vec{\Delta} = (\Delta_1, \Delta_2, \Delta_2)$. To guarantee that each seed converges to the phase that we want, we first run the self-consistent loop by symmetry-restricting the mean-field parameters to have the symmetry they initially have. Once convergence has been reached, we run unrestricted self-consistent loops whose seeds are the solutions of the restricted loops.

4. Additional $T - x$ phase diagrams

In this section we discuss phase diagrams for different gaps and interaction strengths. The main goal of this section is to provide further support to the claim that the existence of C_3 -breaking phases is qualitatively robust.

In our simplified effective model with a given initial gap E_g , it is not possible to choose a value of the interaction that reproduces both the critical temperature T_c and the critical doping x_c for the disappearance of the CDW. Our aim is not to reproduce these values quantitatively (which would require including physics well beyond our model like electron-phonon coupling [68], doping-dependent screening, the effect of the substrate [49, 69], fluctuation corrections to mean field [70] . . .), but rather to show the generic existence of C_3 -breaking phases. Because of this, we choose interaction strengths to match the critical doping above which the commensurate CDW dies and present the phase diagrams as a function of T/T_c , noting that T_c generally changes for different values of E_g . The critical doping we take is $x_c \sim 0.06e/\text{f.u.}$, as seen experimentally [32, 35, 46, 53]. This is an approximate estimate, since at this doping there is a crossover to an incommensurate CDW, where the ground state consists of commensurate domains separated by domain walls [32, 33, 71, 72].

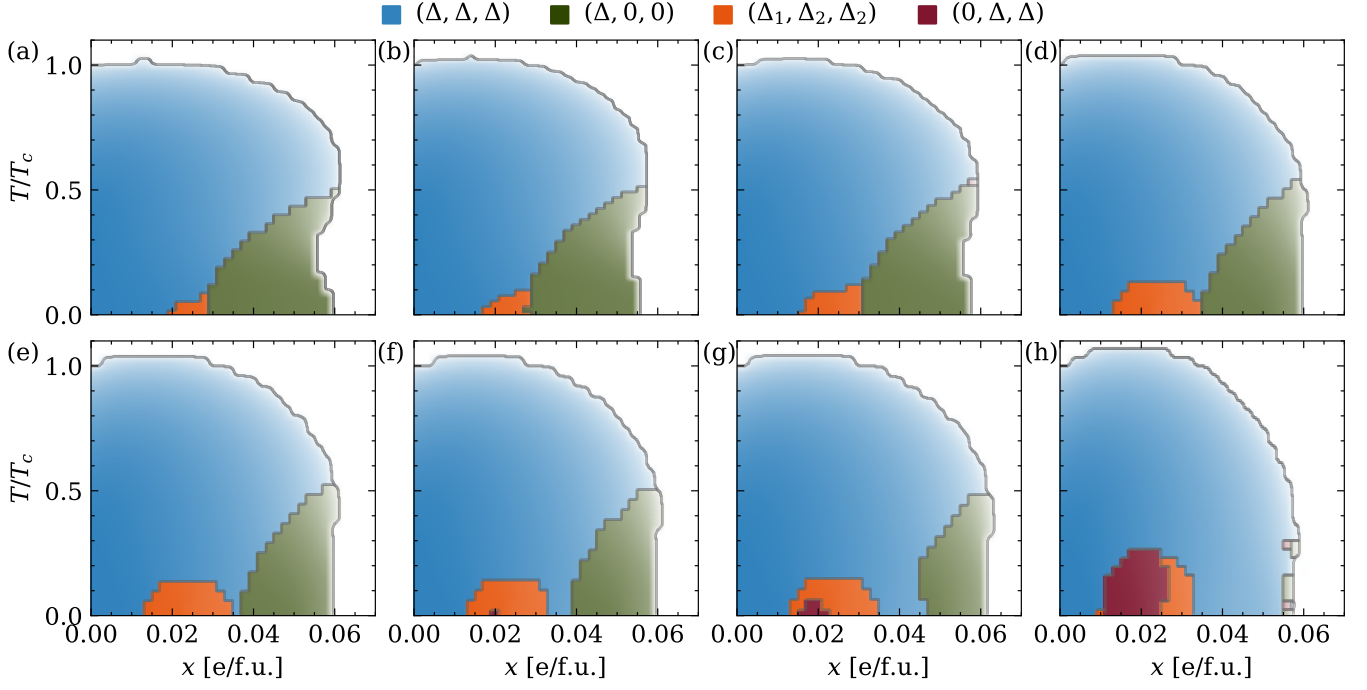


Figure S2. Temperature-doping phase diagrams obtained by self-consistently solving the mean-field Hamiltonian of Eq. (D3):

- (a) $E_g = +50\text{meV}$, $V_{dp} = 890\text{meV}$, $T_c = 576\text{K}$;
- (b) $E_g = +25\text{meV}$, $V_{dp} = 845\text{meV}$, $T_c = 459\text{K}$;
- (c) $E_g = 0$, $V_{dp} = 800\text{meV}$, $T_c = 378\text{K}$;
- (d) $E_g = -25\text{meV}$, $V_{dp} = 740\text{meV}$, $T_c = 269\text{K}$;
- (e) $E_g = -27.5\text{meV}$, $V_{dp} = 733\text{meV}$, $T_c = 259\text{K}$;
- (f) $E_g = -30\text{meV}$, $V_{dp} = 725\text{meV}$, $T_c = 249\text{K}$;
- (g) $E_g = -35\text{meV}$, $V_{dp} = 716.5\text{meV}$, $T_c = 239\text{K}$;
- (h) $E_g = -50\text{meV}$, $V_{dp} = 650\text{meV}$, $T_c = 145\text{K}$.

Taking this into account, Fig. S2 shows how the T - x phase diagrams evolve from gap $E_g = +50\text{meV}$ to $E_g = -50\text{meV}$. The most prominent feature is the shift of the $1Q$ stripe phase to higher doping for decreasing gap, until this phase disappears. This is consistent with the $\mathbf{k} \cdot \mathbf{p}$ predictions of Figs. 2(c,d), which show that the doping above which the $1Q$ solution is more stable than the $3Q$ increases with decreasing gap. Furthermore, while the $3Q$ nematic and the $1Q$ stripe phases share a boundary for positive gaps, they separate for negative gaps, clearly indicating that the origin of these two phases is different, which agrees with our theory. Finally, the relative extension of the $2Q$ phase with respect to the $3Q$ nematic phase increases with decreasing gap.